ACTUATORS

Dual high-stroke and high–work capacity artificial muscles inspired by DNA supercoiling

Geoffrey M. Spinks[1]*, Nicolas D. Martino[1], Sina Naficy[2], David J. Shepherd[1], Javad Foroughi[1]

Powering miniature robots using actuating materials that mimic skeletal muscle is attractive because conventional mechanical drive systems cannot be readily downsized. However, muscle is not the only mechanically active system in nature, and the thousandfold contraction of eukaryotic DNA into the cell nucleus suggests an alternative mechanism for high-stroke artificial muscles. Our analysis reveals that the compaction of DNA generates a mass-normalized mechanical work output exceeding that of skeletal muscle, and this result inspired the development of composite double-helix fibers that reversibly convert twist to DNA-like plectonemic or solenoidal supercoils by simple swelling and deswelling. Our modeling-optimized twisted fibers give contraction strokes as high as 90% with a maximum gravimetric work 36 times higher than skeletal muscle. We found that our supercoiling coiled fibers simultaneously provide high stroke and high work capacity, which is rare in other artificial muscles.

INTRODUCTION

Miniaturization of robotic systems is hampered by conventional mechanical drive systems that are difficult to downsize without loss of performance (*1*). Artificial muscles are seen as viable actuators when size and space are limited because these materials act by direct-drive mechanisms, they have uncomplicated structures, and their performance can be scale independent. Artificial muscle materials can be configured to generate tensile (*2*), bending (*3*), or torsional responses (*4*), and all have found application in prototype robotic devices (*4*–*6*). Tensile artificial muscles are often benchmarked against mammalian skeletal muscle with high stroke, fast response, and high work and power densities as the most desirable characteristics (*7*). However, muscle is not the only mechanically active system found in nature, and here, we draw inspiration from DNA supercoiling, where the double helix bends and folds into higher-order structures with a concomitant reduction in end-to-end length as an alternative mechanism to inspire high-performance artificial muscles (Movie 1).

DNA is one of the stiffest and longest natural polymers, yet in eukaryotic cells, centimeters of DNA are condensed to fit into the micrometer-sized cell nucleus. Such packing is achieved in part through a series of orchestrated supercoiling events (*8*) as can be induced by exposing the DNA to intercalating dyes (*9*–*13*). Here, we evaluate experimental data of Gunther *et al.* (*13*) from experiments on a single 11.3–kilo–base pair plasmid DNA molecule, where supercoiling by intercalation at a binding concentration of 0.1 dye per base pair caused plectoneme supercoiling and the end-to-end length to decrease by ~3 μm when subjected to a constant tensile force of 0.5 pN. This contraction equates to a stroke of more than 80% of the contour length and a contractile work of 1.5×10^{-18} J, which is a gravimetric work of contraction of 0.123 J g^{-1} based on an average base pair molecular weight of 650 g mol^{-1} or 0.103 J g^{-1} when the molecular mass of the dye is included. The mass normalized work capacity of this supercoiling DNA is more than two times higher than that of skeletal muscle (*7*) and suggests supercoiling as a potent mechanism for powering high-stroke artificial muscles.

Understanding how intercalation induces supercoiling in DNA can provide a guide for developing biomimetic artificial muscles. Intercalating dye molecules stack between π-π base pairs in double-stranded DNA, causing unwinding when the DNA ends are torsionally unrestrained (*11*) or supercoiling when the DNA is tethered against rotation (*12*). In the latter, the DNA molecule becomes torsionally energized, with the elastically stored torsional shear energy increasing with the square of the blocked free-end rotation. A buckling transition can ensue by converting twist to writhe with a loop forming in the molecule to give a net lower potential energy. The same fundamental mechanics describe the snarling of textile fibers and hockling of cables and are easily demonstrated by twisting an elastic fiber and bringing the ends toward each other (Fig. 1). Plectonemes are produced as the fiber plies around itself after initial loop formation (Fig. 1A) or if higher axial loads are applied the loops stack into solenoids (Fig. 1B). Plectonemes have been observed in surface-tethered DNA molecules when treated with intercalating dyes (*12*), and a closely related phenomenon occurs in closed circular DNA

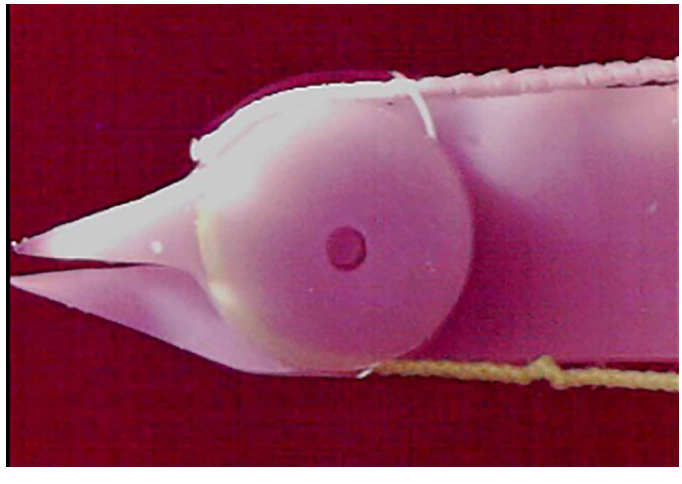

Movie 1. Overview of supercoiling muscles with demonstration actuated microtools.

[1]Australian Institute for Innovative Materials, University of Wollongong, Wollongong, NSW 2522, Australia. [2]School of Chemical and Biomolecular Engineering, University of Sydney, Sydney, NSW 2006, Australia.
*Corresponding author. Email: gspinks@uow.edu.au

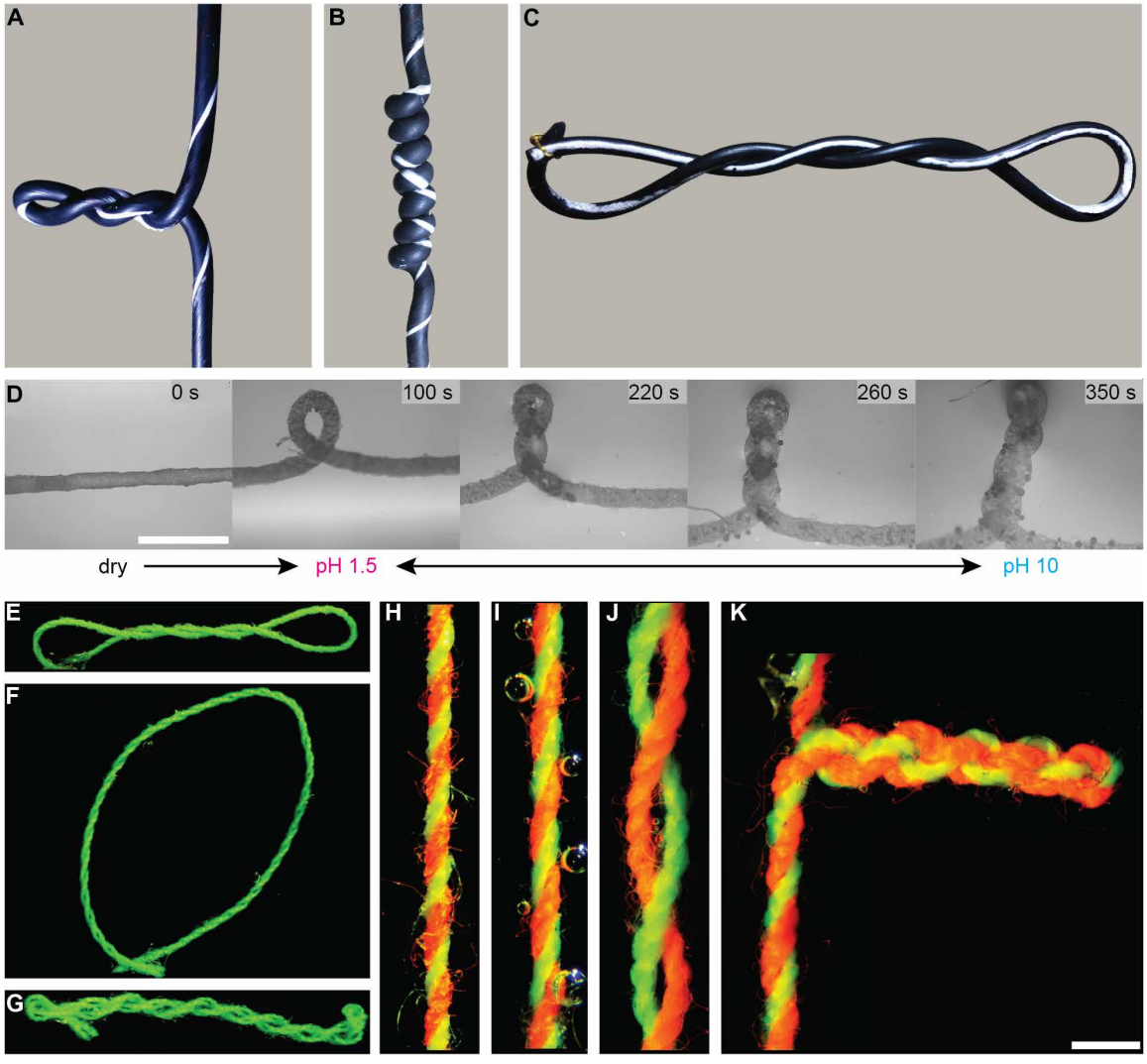

Fig. 1. Examples of supercoiling fibers produced by twist insertion or by swelling. An elastomeric fiber is twisted at a low tensile load to form plectonemes (**A**) or at high load to form solenoids (**B**) or twisted and joined to form a loop (**C**). A series of photomicrographs in (**D**) show a twisted bundle of electrospun and cross-linked PAA nanofibers attached at both ends to a glass slide and immersed from dry in acid (pH 1.5) and then base (pH 10) solutions to form plectoneme. Scale bar, 0.52 mm. Photographs in (E) to (G) show a composite sample prepared from two polyester threads plied and infused with cross-linked PAA, swollen in acid solution, and joined into a loop (**F**) and when fully dried (**E**) and after immersion in base (**G**). A similar sample prepared with two different colored threads is shown in the as-prepared dry state (**H**), after free swelling in acid (**I**) and base (**J**) and in base with the ends tethered against torsion and with a constant isobaric stress of 200 kPa (**K**). Scale bar, 1 mm (H to K).

(*14*), as reproduced in Fig. 1C, where a twisted elastic fiber was joined into a loop and allowed to relax to a plied plectoneme.

The large-scale unwinding of DNA by intercalators is also seen in highly twisted textile yarns in response to volume expansion caused by solvent absorption, heat, or electrochemical charging (*4*, *15*–*23*). However, there have been no previous reports of swelling-induced supercoiling in macroscopic fibers. Here, we introduce actuators that demonstrate reversible interchange between extended linear and supercoiled topologies. Through experiment and application of kinematics, we exploit scaling effects and manipulate boundary conditions to develop supercoiling muscles with high stroke, high work density, and fast and stable responses. These supercoiling muscles are fundamentally different from recent demonstrations of coiling in macroscopic ribbons and fibers (*24*–*28*) where at least one end of the ribbon or fiber was free to rotate so the mechanical work output was zero. Our supercoiling muscles also differ from twisted and coiled tensile actuators (*29*) because these systems retain a supercoiled structure in both their extended and contracted states.

RESULTS

Our first experiments used twisted yarns of several tens of micrometers in diameter that were made from electrospun cross-linked poly(acrylic acid) (PAA) and were swollen in aqueous solutions of either high or low pH with the yarn ends adhered to a glass slide. PAA is a pH-sensitive hydrogel, and initial swelling of the dry fiber in acid solution generated a plectoneme loop that added more turns with further swelling in base (Fig. 1D and movie S1). These additional plectoneme turns dissolved when the yarn was deswollen in acid, demonstrating the reversibility of the swelling-induced supercoiling.

Similar to DNA, the swelling of the PAA yarns with one yarn end torsionally unconstrained confirmed a high degree of untwisting and lengthening. The torsional stroke was 350° mm^{-1} (fig. S1) or about 50% of the initially inserted twist, and the yarns also increased in length by 20% during untwisting. The combined lengthening and untwisting contributed to plectoneme formation when the yarn was fixed at both ends.

The handedness of the supercoiled plectonemes is governed by the Calugareanu (*30*), White (*31*), and Fuller (*32*) relation

$$L_k = T_w + W_r \quad (1)$$

where L_k is called the linking number and represents the number of times the yarn end is rotated, T_w is the twist or number of turns in the yarn, and W_r is the writhe that is related to the out-of-axis bending and the number of crossings the yarn makes with itself. Torsionally tethering the yarn by attaching to a substrate or by forming the yarn into a single loop means that L_k must be conserved. In such circumstances, any change in T_w must be matched by an equivalent change in W_r but of the opposite sign. Writhe is a directional property so that plectonemic and solenoidal supercoils having the same writhe will have opposite chirality (*14*). This curious feature is illustrated in Fig. 1, where the plectonemes introduced by twisting the elastic fiber at low tension are the opposite hand to the twist direction, whereas the solenoids formed at high loads have the same handedness as the inserted twist. It is then apparent using this framework that the appearance of left-handed plectonemes by swelling of the right-hand twisted PAA yarn is positive writhe arising from yarn untwisting. The same phenomenon occurs by intercalation of DNA where plectonemes of opposite chirality arise from partial unwinding of the molecule.

Because the PAA nanoyarns could not sustain high tensile loads without fracture, we next developed high-strength hydrogel composites using textile fibers as reinforcement. Most testing was performed on plied composites formed by twisting two polyester threads infused with cross-linked PAA. Reversible supercoiling was confirmed by first mimicking plectoneme formation in circular DNA. The example of Fig. 1 (E to G) (and movie S2) used a composite fiber swollen in acid solution with free untwist and then formed into a relaxed loop secured with a small amount of adhesive. Additional swelling in base generated plectonemic supercoils with a left-handed chirality, confirming the further untwisting of the right-hand twisted composite fiber. This supercoiling was eliminated by immersion and deswelling in acid, and the continued volume contraction and uptwist on drying generated a new right-handed plectoneme. A composite fiber prepared with contrasting colored threads illustrates the twisted double helix of the two-ply structure in the dry state (Fig. 1H) and after free swelling in acid (Fig. 1I) and base (Fig. 1J). Torsionally tethering an identical sample in the dry state but allowing it to contract in length produced a multiple-loop plectoneme (Fig. 1K and movie S3) when immersed in base and where sufficient space perpendicular to the fiber was available to allow unimpeded plectoneme growth. This supercoiled structure remained stable for as long as the sample ends were restrained against rotation. The isobaric contraction strain for this sample at an applied tensile stress of 200 kPa was 70.5% of the dry length, and the gravimetric work of the contraction cycle was 0.2 and 0.04 J g^{-1} based on the sample dry mass and fully swollen mass, respectively. Even this nonoptimized sample generated impressive actuation, with up to three times higher stroke and at least equivalent work capacity of mammalian skeletal muscle (*7*).

Modeling of swelling-induced supercoiling

Exploiting this supercoiling phenomenon to drive high–work capacity artificial muscles was guided by kinematic theory. We first developed a geometrical analysis to predict untwist by free swelling of our composite fibers (Fig. 2). Swelling in the direction perpendicular to the fibers was assumed to be the same as the one-dimensional

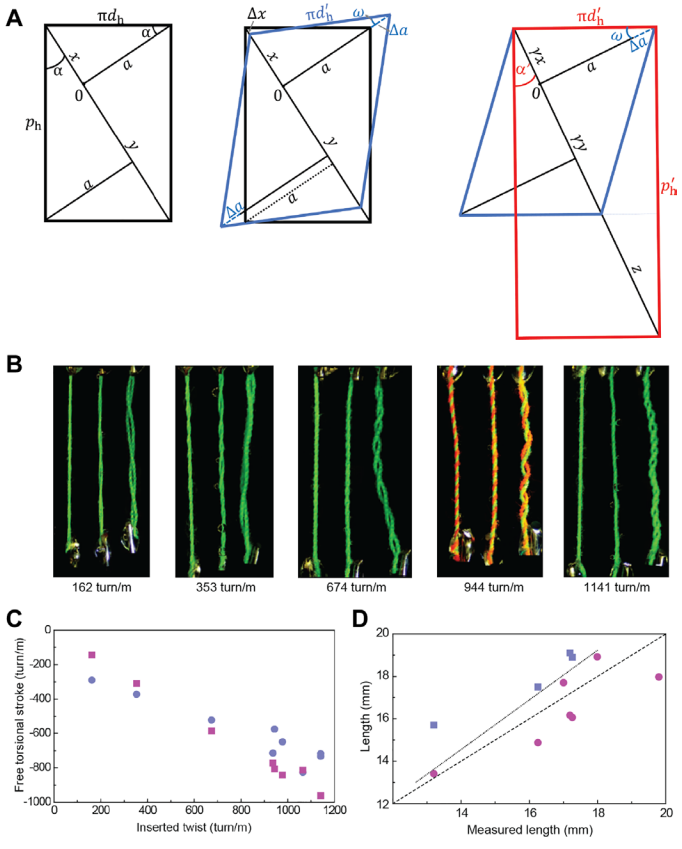

Fig. 2. Torsional actuation in polyester-PAA composite fibers. (**A**) Two-dimensional representations of plied composites where the cylinder defined by the centerline of one thread in the composite is conceptually cut along its long axis and rolled out to a rectangle. Left: The geometry of one turn in the plied sample before swelling is shown by the black rectangle with diameter d_h and pitch p_h. Center: Swelling occurs perpendicular to the thread direction along line *a*, whereas contraction occurs along the thread direction shown by lines *x* and *y* to distort the original rectangle to the blue parallelogram. Right: The red rectangle represents the opened-up two-dimensional view of the swollen cylinder. The new sample diameter and pitch are indicated by d'_h and p'_h, respectively. The helix angle changes from α to α', and the helix path length increases from $x+y$ to $\gamma(x+y)+z$ where γ is the ratio of the thread length after swelling to the dry thread length. (**B**) Images of two-ply composite samples with different starting inserted twists as indicated. Each panel shows an image of the sample in the initial dry state (left) and after immersion in acid (middle) and base (right). Samples were allowed to freely swell and rotate without any applied tension or torque. (**C**) Torsional stroke after free swelling of polyester-PAA composite fibers prepared with different inserted twists and swollen from dry in base solution (pH 13). Measured (circles) and calculated torsional strokes (square symbols) are shown. (**D**) Comparison of calculated and measured sample length after free swelling in base. Squares are calculated values assuming no change in thread length, and circles are calculated values using the measured thread length ratio of $\gamma = 0.85$. The dotted line indicates the dry length and is included for comparison with the lengths after immersion in base. The dashed line shows the equivalence between calculated and measured values.

free swelling of the hydrogel matrix, which was λ = 2.5 for cross-linked PAA having a measured mass swelling ratio of 16.5 (≈λ^3). The dimensional change due to swelling along the fiber direction was measured in a single PAA-impregnated polyester thread as γ = 0.85. As described in the Supplementary Materials (equations S26 to S36), the swelling-induced torsional stroke normalized to the sample dry length is

$$T_o = T\left[\gamma\left\{\frac{1+\left(\frac{1}{\tan\alpha}\right)^2}{[(\lambda\cos\alpha)^2+(\gamma\sin\alpha)^2]\left[1+\left(\frac{\lambda}{\gamma\tan\alpha}\right)^2\right]}\right\}^{1/2}-1\right] \quad (2)$$

where T is the initially inserted twist per dry sample length and α is the initial twist angle at the fiber surface. Measurements confirmed that free untwist increased in magnitude with inserted twist (Fig. 2, B and C) with very good agreement between the measured and predicted free torsional strokes, as was the prediction of the final sample length (Fig. 2D). The composite sample prepared with the highest initial twist of 1140 turns m^{-1} had a fractional torsional stroke of −65% or 250° mm^{-1}, which compares favorably with other solvent-driven torsional actuators, including polymer-coated twisted carbon nanotube yarns that generated a torsional stroke of 143° mm^{-1} or −55% of the initial twist (*21*).

Theoretical description of fiber length change due to supercoiling was based on previous analysis of DNA molecules (*33*–*39*) and long, slender rods in general (*40*–*49*). Detailed and sophisticated numerical modeling described recently (*49*) provides comprehensive analysis of supercoiling, but a simpler analytical approach was used here to aid understanding of the underlying mechanisms. As described in the Supplementary Materials, the fractional reduction in muscle end-to-end length (ΔL) due to supercoiling by adding twist (T_o) at a constant tensile force (F_x) and when normalized to the muscle contour length (S) is

$$\frac{\Delta L}{S} = \left(T_o - \frac{\pi}{S}\right)\sqrt{\frac{B}{2F_x}} - \frac{B}{C} \quad (3)$$

where B and C are the bending and torsional stiffnesses, respectively, and twist is expressed in radians per muscle length. The comparison of calculated and experimentally measured tensile actuation strains is shown in Fig. 3A and fig. S2 for a typical composite sample. With further modification to account for self-contact and non-coiling contributions to contraction, the calculated tensile strokes were found to be in good agreement with measured values. Actuation strains decrease in magnitude with increasing externally applied load, because the twist needed to induce coiling increases and the loop diameter decreases. The model predicts the elimination of coiling at applied tensile stresses above 830 kPa, which is close to the experimentally observed coiling limit of 1000 kPa. The model also predicted the formation of a five-turn plectoneme at an applied stress of 180 kPa, which concurs with the top microscopic image in Fig. 3B. Solenoids form at higher loads when the coil diameter is reduced to the same magnitude as the fiber diameter, as shown by the bottom microscope image in Fig. 3B at 900 kPa and in movies S4 and S5.

The theory predicts that supercoiling contraction strains are larger whenever the available twist (T_o) increases (fig. S2D), as was confirmed by experiments that show higher tensile strokes measured from samples prepared with more twist and similar diameters (Fig. 3C). The larger torsional stroke generated from the swelling of highly twisted samples has the main effect of extending the coiling region to higher stresses with concomitantly higher actuation strokes. The sample prepared with the smallest twist of 183 turns m^{-1} did not show any coiling actuation even when tested isotonically at a small tensile force of 10 mN (53 kPa), whereas the sample having an initial twist of 942 turns m^{-1} generated solenoidal supercoils even at stresses up to 1000 kPa. A higher inserted twist generates a higher torsional stroke on swelling so that more coils can form. In addition, a higher twist reduces the ratio of bending to torsional stiffness (fig. S3) and lowers the energy cost of bending so more supercoil turns can form.

The validated tensile actuation model was then used to investigate scaling effects. As expected, the change in sample dry length had negligible impact on the tensile strain at any given isobaric stress (fig. S2B). However, a change in sample diameter had a strong effect, with increasing tensile actuation strain at a given tensile stress confirmed from experiments where samples were prepared from different numbers of polyester threads and twisted to the same degree (Fig. 3D). The model predicted an increasing actuation strain in samples with larger starting diameters (fig. S2C). This trend is expected because an increase in swollen sample diameter increases the bending stiffness without changing the ratio of bending to torsional stiffness, so that the twisting threshold for first coil formation is reduced (equation S18). In addition, an increased bending stiffness favors a larger coil diameter (equations S17 and S20), so the combined effects contribute to a larger coiling-induced actuation strain in isotwist samples of increased diameter.

More twist can be inserted into fibers of small diameter; thus, investigating whether higher performance supercoiling muscles arise from higher twist/smaller diameter fibers or lower twist/larger diameter fibers should be explored. The maximum twist that can be inserted increases by twisting against higher tensile loads and is capped by coiling at an applied stress limited by the material's tensile strength (σ_T). The critical twist for coiling depends on the sample length (S), diameter (d), and elastic moduli (E and G)

$$T_c = \frac{\pi}{S} + \frac{\sqrt{E\sigma_T}}{dG\sqrt{2}} \quad (4)$$

This relation shows that the maximum inserted twist ($T = T_c$) scales with the inverse of fiber diameter if the tensile strength is diameter independent. The surface twist angle at this maximum inserted twist is also independent of diameter because tan α = πdT. According to Eq. 2, the torsional stroke will now scale directly with inserted twist and increase with the inverse of the sample diameter. However, the increasing torsional stroke with decreasing fiber diameter will be canceled by the reduced coil radius, so that samples that are twisted to the maximum extent and swollen at equivalent isobaric stresses should exhibit identical tensile strains and work capacities. It has been noted, however, that materials of smaller dimensions have higher tensile strengths, and it is yet to be seen whether this feature could be exploited to insert higher twist and produce enhanced supercoiling actuation.

Combining high stroke with high work capacity

Our composite polyester-PAA supercoiling muscles generated some of the highest tensile strokes reported to date at 80% of the dry length, which is at least double the stroke of mammalian skeletal muscles (*7*). Similarly, high strokes of 70 to 80% have also been reported from hygromorph muscles made from spring-like coils (*18*, *50*, *51*). These twisted and coiled fibers also generate exceptionally high torsional strokes of 600° to 1200° mm^{-1} (*18*, *51*, *52*), so we

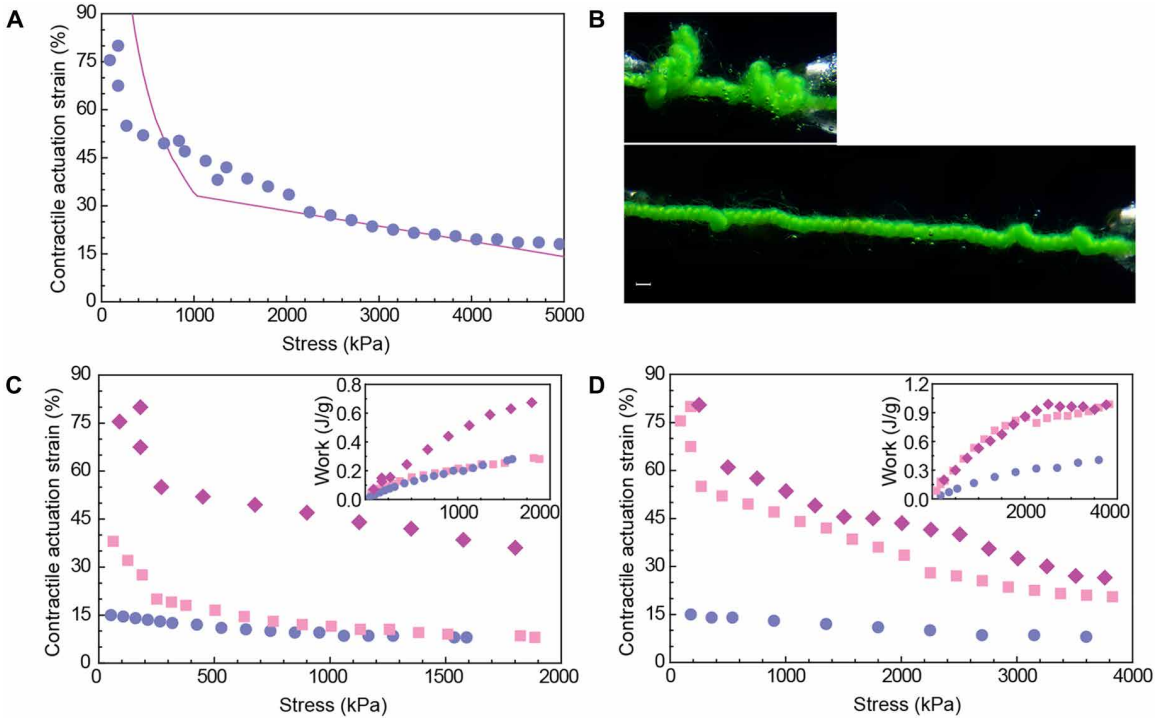

Fig. 3. Tensile actuation in polyester-PAA composite fibers. (**A**) Tensile actuation strains measured at various isobaric stresses (symbols) and predicted from theory (line). (**B**) Photomicrographs show the sample equilibrated in base solution at 180 kPa (top) and 900 kPa (bottom) with the scale bar equivalent to 0.4 mm. (**C**) Measured actuation strains and work capacity as a function of isobaric stress for samples prepared with different inserted twists: 183 turns m^{-1} (circles), 406 turns m^{-1} (squares), and 942 turns m^{-1} (diamonds). (**D**) Measured actuation strains and work capacity as a function of isobaric stress for samples prepared with different starting diameters: 0.27 mm (circles), 0.38 mm (squares), and 0.50 mm (diamonds).

investigated whether coiled fibers could generate sufficient torque to produce coiled coil structures. A two-ply polyester-PAA ribbon was overtwisted to form a solenoidal supercoil that was set by thermal cross-linking. Swelling of this sample by immersion in base solution generated a strain of 15 to 20% at isobaric stresses above 2000 kPa (Fig. 4A), which was due to the change of the intercoil spacing through the untwist of the composite fiber (*29*). In addition to this baseline actuation, a "high-gear" response with contraction strains of up to 90% of the dry, unloaded length occurred at stresses below 2000 kPa. The additional strain was due to secondary supercoiling where the coiled fiber was further coiled into plectonemes. The maximum work capacity of this sample was 1.45 J g^{-1} based on the dry mass or 0.35 J g^{-1} when normalized to the fully swollen mass. Given an enthalpy of protonation of PAA of ~3.7 kJ mol^{-1} (*53*), the maximum chemomechanical coupling efficiency is 14%. The coiled coil contribution to the tensile stroke boosts the work capacity of the muscle in the high-stroke regime, which is highly unusual—work output ordinarily decreases toward zero with decreasing stress because the change in actuation strain cannot compensate for the change in applied load. This typical behavior was seen in our composites that were not coiled and for our coiled coil samples when tested at stresses above 2000 kPa. Recent examples of high-stroke hygromorphs (*18*, *50*), as well as other actuators such as twisted and coiled fibers (*21*) and electrohydraulic transducers (*54*), all show the typical performance trade-off, with high stroke achieved only with a low work output and high work corresponding to low strokes. In contrast, our coiled coil muscles show an unusual peak in the work output at intermediate stresses, giving strokes of ~70% while maintaining a high work capacity in excess of 1 J g^{-1}. The onset of plectoneme supercoiling greatly enhances the contraction stroke, with a doubling in stroke when the stress was reduced from 1500 to 1000 kPa. The increase in stroke in this regime more than compensates for the reduction in load so that the work output increased. At still lower stresses, however, the increased actuation strain cannot compensate for the reduction in load so that work output again declined.

Speed and stability of supercoiling muscles

The further practical utility of the supercoiling muscles was assessed in terms of cycle lifetime and response time. Reversible large stroke actuation and force generation were observed from multiple swelling and deswelling cycles for a noncoiled composite sample (Fig. 4B and fig. S4). The acid-base actuation was stable with a reversible stroke amplitude of 35% that varied by less than 7% over 32 cycles. To reduce actuation times, we prepared composite yarns of small diameter by cotwisting electrospun bundles of PAA and polyacrylonitrile (PAN) nanofibers. In the example shown in Fig. 4C, a multiturn plectoneme contracted to more than 90% of the dry length when immersed in base and with an applied isobaric stress of 200 kPa. The transition from acid to base solution occurred mostly within the first 4 min with a contraction strain from acid of 66% and an average contractile strain rate of 0.27% s^{-1}. It is noted that an additional small contraction in length occurred during the transition from base to acid solution that was caused by drainage of the bath and brief exposure of the sample to air. In general, the length expansion by hydrogel reprotonation by reimmersion in acid was always

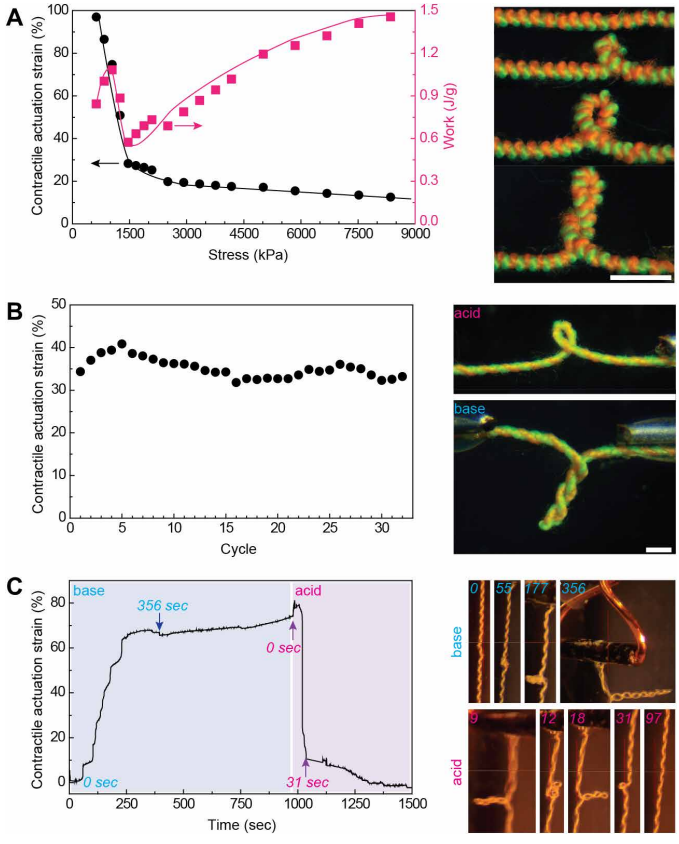

Fig. 4. High–work capacity, stable, and fast supercoiling artificial muscles. (**A**) Actuation strains and gravimetric work capacities measured at various isobaric stresses for a coiled two-ply polyester-PAA sample. Photomicrographs illustrate the coiled coil plectoneme formation in base solution. Scale bar, 1.75 mm. (**B**) Actuation strain amplitude measured by sequential immersion in acid (pH 1) and base solutions (pH 13) over 32 consecutive cycles with photomicrographs showing the sample after equilibration in each solution. Scale bar, 1 mm. (**C**) Time trace of actuation strain during immersion of PAN-PAA twisted nanoyarns in base (pH 10) from acid solution (pH 1.5) with photomicrographs taken at the indicated times.

faster than deprotonation in base (movie S6). For the electrospun nanoyarns, an expansion of 63% occurred in only 24 s, giving an average expansion strain rate of 2.63% s^{-1}. The peak expansion strain rate was up to 50% s^{-1} when several plectoneme coils were removed during only 1 s, as illustrated in movie S7, although this rapid expansion may be aided by the applied load or factors such as the sudden release of intercoil friction. For comparison, the hybrid carbon nanotube twisted and coiled hygromorphs reported by Kim *et al.* (*50*) generated an average contractile rate of 3.95% s^{-1} when prepared to a diameter of only 50 μm and when the dried sample was exposed to high humidity. Reducing fiber diameter is a successful means to increase actuation rate, but it comes with a reduced force output. To overcome this limitation, we prepared simultaneously fast and strong muscles by assembling a five-strand parallel PAA-PAN array giving a stroke in excess of 60% with a fast response (2% s^{-1}) at an isobaric stress of 180 kPa (movie S8).

DISCUSSION

In summary, we report a new class of tensile artificial muscles that operate by converting twist in straight fibers to writhe. Very large length contractions of up to 90% have been demonstrated with coiled coils giving simultaneously high work capacity and high strokes. The twist inserted and trapped in the fibers during manufacture acts as a latent source of mechanical energy that can be activated by swelling and restored by deswelling. These volume changes can be induced chemically, as in the present study, or by other means, including thermal, photonic, sorption, and electrochemical. The supercoiling mechanism can operate in any composite fiber containing helically oriented reinforcing filaments and can be scaled from molecular to macroscopic dimensions. To aid the development of supercoiling muscles, we introduced a two-stage theoretical model for the prediction of the torsional actuation of untethered fibers and the length change when the same fibers were torsionally tethered. The model correctly predicts scaling effects arising from inserted twist and fiber dimensions and suggests that further improvements in supercoiling muscle performance could be achieved in small-diameter, high-strength twisted fibers. Further work can also consider swelling kinetics for a dynamic model of the supercoiling muscles to allow for enhanced control of these actuators in robotic systems.

The burgeoning interest over the past decade in soft robotics has been accelerated by the introduction of new actuation systems that provide useable mechanical outputs and are accessible to the wider robotics community (*55*). Supercoiling muscles are expected to provide further opportunities in the development of insect-like robots, wearable assistive devices, micromanipulators, and miniature surgical tools. To assess their usability as micro-actuators we fabricated miniature scissors and tweezers by 3D printing (fig. S6). With attached short lengths of 2-ply composite polyester–PAA yarns, we could demonstrate complete closing and reopening of the microtools by successive immersion in base and acid solutions, respectively (fig. S7). The supercoiling muscles share an inherently low cost and ease of fabrication with twisted and coiled polymer fiber muscles, with the latter being extensively adapted for a myriad of robotic applications since their introduction in 2014 (*56*–*58*). Supercoiling muscles offer an additional ultrahigh strain regime that is inaccessible to twisted and coiled muscles without sacrificing work capacity. Extending the currently demonstrated chemoresponsive supercoiling muscles to electrothermal devices using electrically conductive yarns and thermosensitive matrices allows immediate adaptation to many soft robotic applications. Furthermore, environmentally responsive matrices could power supercoiling muscles for autonomous and self-powered devices, such as controlled drug release in the gastrointestinal tract or for humidity-controlled textiles in clothing to aid thermal comfort.

Unlocking the mechanisms used in nature provides continued inspiration for advancing materials (*59*). Here, we observed that the dynamic behavior of our composite fibers closely mimics the supercoiling of DNA by intercalators. This phenomenon occurs without the insertion of additional twist and differs from the common experience with cables and strings where writhe is produced by twisting. Our systems may function as simple prototype educational aids or even to assist in the further study of DNA. Our theory for the fractional length changes by supercoiling was found to reasonably predict the measured length of a single DNA molecule during twist insertion at constant tension (fig. S5A), and our models of swelling-induced torsion may be further developed to predict the unwinding and overwinding of DNA by intercalators or metal ions. Supercoiling processes also occur in other biological systems, including the fast coiling of *Vorticella*'s stalk (*60*), twining of vines and plant tendrils (*61*), and protein action on neuronal microtubules (*62*). All of

these examples incorporate helically oriented fibers that are stimulated to coil by changes in volume and can inspire the further development of synthetic systems for micromotors based on twist-to-writhe conversions for a fascinating array of robotic actions.

MATERIALS AND METHODS

Sample preparation

The most commonly used sample was constructed from two polyester threads infused with cross-linked PAA. The two-ply samples were prepared by arranging the two polyester threads [100% spun polyester sewing thread (Birch Haberdashery & Craft), supplied as two-ply Z twist from staple fiber yarn] on a flat plastic board and affixing the threads at both ends with adhesive tape with sufficient tension to hold the threads straight. The threads were arranged parallel to each other with a small separation of ~0.5 mm. Next, a 10 weight % (wt %) solution of PAA (average molecular weight, 1,800,000 g mol^{-1}; Sigma-Aldrich, Australia) in dimethylformamide (Sigma-Aldrich, Australia) was injected to fill the gap between the polyester threads, and the solvent was evaporated by oven heating at 60°C. The injection of PAA solution was repeated, and the solvent again evaporated. Twist was then inserted into the polyester-PAA ribbon by first attaching metal hooks to the ribbon ends using ultraviolet (UV)–curable adhesive. The length of the ribbon was measured, and then the ribbon was suspended vertically from the shaft of a DC motor. A weight was attached to the ribbon's free end with light contact with a vertical board to prevent weight rotation during twisting. For a two-ply composite, the weight was 112 g, and the tensioning weight was adjusted in proportion for other multiply samples. Twist was inserted in a *Z* direction using the DC motor with turns counted. The length of the sample was checked periodically during twisting to achieve the desired inserted twist, which was the number of turns inserted normalized to the twisted sample length. After twisting, the sample was removed from the DC motor and transferred to a frame for oven curing. Tension was maintained during transfer to the frame and after attaching the sample to the frame to prevent coil formation. The samples were cured by cross-linking the PAA with Jeffamine ED600 (Sigma-Aldrich, Australia) that was incorporated into the PAA solution in a weight ratio of 3.6% Jeffamine to PAA. The Jeffamine is *O*,*O*′-bis(2-aminopropyl) polypropylene glycol–*block*–polyethylene glycol–*block*–polypropylene glycol with a molecular weight of ~600 g mol^{-1}. After curing for the specified time, the sample was removed from the oven and allowed to cool. At this stage, the twist inserted in the sample was trapped by the cross-linked PAA. The samples were stored at ambient laboratory conditions.

Samples were prepared for testing by cutting a small length (typically 10 to 40 mm) and attaching metal hooks to both ends with UV-curable adhesive. This sample was then attached to a perspex frame, and the sample was immersed in base solution (0.1 M NaOH in distilled water) for 1 hour. Surface gel was then manually removed, and the sample was immersed in acid solution (0.1 M HCl in distilled water) for 20 min. The sample was then dried. The composite fibers incorporated ~20 wt % PAA, and a PAA film cross-linked in the same manner as the composites gave a mass swelling ratio compared with the dry mass of 3.2 when immersed in 0.1 M HCl acid solution and 16.6 when immersed in 0.1 M NaOH base solution. Unless otherwise noted, the tensile stresses and strains are reported with reference to the dry, unloaded diameter and length, respectively.

Small diameter samples were also prepared from electrospun fibers of PAA or composites of PAA and PAN (average molecular weight, 1,500,000 g mol^{-1}; Sigma-Aldrich, Australia). Aligned nanofibers were first prepared by collecting the electrospun fibers as a film suspended between two rotating parallel disk electrodes (fig. S8). Periodically, the film was collected into a bundle using a collector consisting of a second stationary set of parallel disks. The proportion and final diameter of the twisted bicomponent yarns could be controlled by adjusting the electrospinning times. For example, a yarn with a dry diameter of 106 μm with a volume ratio of PAA to PAN of 2:1 was prepared by electrospinning the PAA-ED600 mixture for 6 min and the PAN for 1 min. The collected bundle was then twisted to 2000 turns m^{-1} and thermally cross-linked at 130°C for 6 hours. Figure S8C shows an electron micrograph of the prepared sample.

Tensile actuation and tensile stiffness

The tensile properties of the supercoiling muscles were evaluated by loading and unloading in the dry state and after immersion in acid or base solutions. The in-house–constructed tensile testing instrument consisted of a rigid frame supporting a screw-driven crosshead. The crosshead displacement was measured directly using a linear voltage distance transducer (Solartron Metrology, model LVDT, ±25 mm range). A cantilever spring was attached to the crosshead, and the cantilever supported a sample clamp. The position of the sample clamp could be shifted along the length of the cantilever spring to allow for adjustments in the force sensitivity. The displacement of the cantilever spring at the clamping point was measured using a noncontact laser displacement sensor (Panasonic HG-C1100) with a range of 70 mm and a sensitivity of 4 μm. Calibration of the testing instrument was performed before all tests. The calibration first correlated the two distance sensors by moving the crosshead without any sample attached to the cantilever spring. Next, the cantilever spring was calibrated by attaching a series of known weights to the clamp. A traveling microscope was used to measure the sample dimensions at various times during testing.

The tensile testing procedure involved both the measurement of the tensile stiffness of the sample in each environment and the isotonic stroke measurements as the environment was changed. The full procedure commenced with the loading and unloading of the sample in the dry state. Next, the sample was loaded to the desired isotonic preload force, and the sample was fully immersed in acid solution. The tensile force acting on the sample was kept constant by adjusting the crosshead position. Loading and unloading of the sample in acid were then followed by isotonic actuation from acid to base by immersing the sample in base. Loading and unloading the sample in base were then performed followed by reimmersion in acid at the same or at a new isotonic force. Several complete isotonic actuation cycles between acid and base solutions were performed at different preloads. Figure S9 shows typical tensile test results where pink, purple, and blue dashed lines in the figure represent the loading and unloading stress-strain curves for the sample tested dry and after immersion in acid and base, respectively. It is noted that a considerable loading/unloading hysteresis occurred for the sample tested in base, and the hysteresis is associated with a higher load to pullout coils than is needed to form coils (*35*, *41*). Four example isotonic test results are also shown in fig. S9A as horizontal lines. Archetypal results are illustrated by the isobaric test at 800 kPa. The sample was loaded to 800 kPa in acid and then transferred to a base solution while maintaining a constant stress. Over

time, the strain decreased due to coil formation and noncoiling actuation. The contraction stroke in this instance was 18%. The sample was then loaded to a maximum stress, unloaded to zero stress, and reloaded to 800 kPa. The reverse actuation from base to acid at the same constant stress generated an expansion strain of 32%, which was considerably larger than the contraction strain. Similar differences in the contraction and expansion strains were observed for all applied stresses and reflect the loading/unloading hysteresis that causes a variation in the starting length of the sample depending on its loading history.

Figure S9B shows a comparison of the isotonic actuation strains measured at different applied stresses and calculated using three different methods. The directly measured isotonic strains are shown as circles in fig. S9B with the larger contraction strain corresponding to the expansion from base to acid and when the starting stress was reached by loading (rather than unloading). The lower actuation strain value at each stress corresponds to the contraction strain occurring when the sample was immersed in base from acid and after the sample was set by loading in acid. The finishing point for the isotonic actuation always lies between the extremes set by the loading/unloading stress-strain curves in acid and base. The square symbols shown in fig. S9B represent the average of the isotonic actuation measured over a full cycle of acid to base and base to acid. The two dashed lines in fig. S9B correspond to the loading and unloading stress-strain curves in base, and the solid line is the average strain difference between the loading and unloading curves at any given stress. This average strain value closely follows the measured average isotonic strains. The reported actuation strains in the main article are the average of the contraction/expansion cycle and were determined by direct isobaric tests supplemented by the averaging of the loading/unloading stress-strain curves.

Torsional actuation and torsional stiffness

The torsional properties of the supercoiling muscles were evaluated by swelling and deswelling the sample while attached in series to a calibrated torsion sensor fiber. Testing included a series of experiments where the torsional stiffness was measured under the dry condition, followed by torsional actuation by immersion in acid or base (fig. S3A). The torsional stiffness test involved first tensioning the connected muscle and torsion sensor fiber to the desired force and measuring the starting angle of rotation of the paddle attached to the torsion sensor fiber. Tensioning occurred by adjusting the crosshead and cantilever spring assembly to which the torsion sensor fiber was connected. Paddle angles were calculated from videographs taken from directly above the sample. Torsional stiffness was measured by the change in rotation of the paddle resulting from manual changes in the rotation of the torsion sensor fiber. The torsion sensor fiber was briefly disconnected from the cantilever spring, rotated one full turn, and reconnected to the cantilever spring. The crosshead was then adjusted to return the tension force to the set value. For descriptive purposes, the torsion sensor fiber is described as attached to the cantilever spring at its proximal end and to the muscle sample at its distal end. The sample rotation (ϕ_M) was calculated from the paddle rotation with the paddle located a distance x from the proximal end of the torsion sensor fiber. Rotation at any point on the torsion sensor fiber (ϕ_x) varies linearly with the distance along that fiber so that

$$\phi_x = \phi_o - \frac{x}{L}(\phi_o - \phi_L) \tag{5}$$

where ϕ_o and ϕ_L are the rotations at the proximal and distal ends, respectively, of the torsion sensor fiber having a length = L. At the distal end where the torsion sensor fiber is connected to the muscle, $x = L$ and $\phi_M = \phi_L$ so that

$$\phi_M = \phi_o - \frac{L}{x}(\phi_x - \phi_o) \tag{6}$$

The torque applied to the muscle and the torsion sensor fiber are of equal magnitude at equilibrium, and the torque (T_M) can be determined from the known torsional stiffness of the torsion sensor fiber ($J_R G_R$)

$$T_M = \frac{J_R G_R}{L}\phi_M \tag{7}$$

The torsion sensor fiber was calibrated by measuring the resonance frequency in torsion of a paddle attached to the fiber. A 103-mm-long piece of 4-lb fishing line (SpiderWire, EZ Mono 4 lb, 0.20-mm diameter) was used for torsional stiffness and torsional actuation measurements unless otherwise stated. A plastic rectangle of 54 mg in weight and 40 mm in length with moment of inertia $I = 7.2\ \text{g mm}^2$ was attached to the fiber at a distance of $L_x = 51$ mm from one end using a small amount of UV-curable adhesive. The torsion sensor fiber was tensioned at 100, 200, 300, or 400 mN, and the paddle was disturbed to initiate self-damped oscillation in torsion. A laser displacement meter (Panasonic HG-C1100) was used to detect the displacement of the paddle from which the period of oscillation (P_o) was measured. The decay in oscillation amplitude was used to calculate the logarithmic decrement (δ), and these values were used to calculate the true torsional period (P)

$$P = \frac{P_o}{\sqrt{1 + \left(\frac{\delta}{2\pi}\right)^2}} \tag{8}$$

The stiffness (S_R) of the torsion sensor fiber was then calculated from

$$S_R = \frac{4\pi^2 I}{P} \tag{9}$$

Last, the torsional stiffness of the torsion sensor fiber was calculated from

$$J_R G_R = \frac{S_R}{\left(\frac{1}{L_x} + \frac{1}{L - L_x}\right)} \tag{10}$$

The shear modulus could then be obtained from the measured radius of the torsion sensor fiber (r_R) because

$$J_R = \frac{\pi r_R^4}{2} \tag{11}$$

Sample dimensions were measured using a traveling microscope. Consistent torsional oscillation periods of $P = 0.258 \pm 0.0003$ s were obtained with no noticeable effect of the applied tensile load. The torsional stiffness was calculated to be $J_R G_R = 0.103 \pm 0.0002\ \text{N mm}^2$. The shear modulus of the torsion sensor fiber was then $G_R = 595 \pm 1$ MPa, which is reasonable for nylon-6.

Typical torsional actuation results are shown in fig. S3A. Immersion of the dry sample in acid solution caused swelling with untwisting rotation of the sample against the torsion sensor fiber. The sample rotation and torque increased with time until equilibrium

was established. The torsional stiffness was then measured by incrementally adding or removing turns to the proximal end of the torsion sensor fiber and measuring the paddle rotation. The twist and torque applied to the sample were calculated using Eqs. 6 and 7, and the slope of the torque versus twist line (JG/L) was converted to torsional stiffness (JG) and shear modulus (G) using the directly measured and environmentally conditioned sample length and diameter. The torsional actuation was then repeated by immersion in base solution, followed by torsional stiffness measurement in base.

Torsional actuation stroke was also measured in a free rotation experiment where the sample was clamped at one end only and fully immersed in the swelling solution without any external tensile load or torque. Video recording of the free sample end rotation was analyzed to determine the torsional actuation stroke. The free torsional stroke measured in this way closely matched the free torsional stroke obtained by extrapolation of the torsional stiffness data when the torsional stiffness was measured at a small tensile load. For example, the free stroke after immersion in base can be estimated by extrapolation of the data given in fig. S3A and when normalized to the sample dry length is −628 turns m^{-1}. This measurement agrees very well with the free stroke of −648 turns m^{-1} determined from the free swelling experiment on an equivalent sample. In a further validation of the two methods, three identical samples were tested either in the free torsion or by actuating against a torsion sensor fiber with a torsional stiffness of either 0.103 or 0.473 N mm^2. The latter torsion sensor fiber was 12-lb fishing line (SpiderWire, EZ Mono 12 lb, 0.3-mm diameter) that was sufficiently stiff to prevent almost all of the torsional actuation and gave a measurement of torque that was close to the blocked torque. Figure S10 shows the combined results from the three experiments with all data points falling on the same torque-twist linear line. The combined results confirm that the torsional actuation ranges linearly from the free torsional stroke to the blocked torque with the slope of the transition governed by the sample torsional stiffness.

SUPPLEMENTARY MATERIALS

robotics.sciencemag.org/cgi/content/full/6/53/eabf4788/DC1
Text
Experimental observation of supercoiling by twist insertion
Theoretical analysis of supercoiling by twist insertion
Experimental validation of supercoiling artificial muscle model
Theoretical estimation of torsional actuation and swelling geometry in plied composites
Swelling-induced dimensional changes without untwist
Effect of inserted twist on the tensile modulus and bending stiffness of two-ply composites
Supercoiling artificial muscle modeling procedure and predictions
Modeling of intercalation-induced DNA supercoiling and twist-induced supercoiling
Demonstration application for supercoiling muscles
Additional supporting experimental data
Appendix: List of definitions, acronyms, and symbols
Fig. S1. Torsional actuation by swelling twisted composite fibers.
Fig. S2. Tensile actuation in polyester-PAA composite fibers.
Fig. S3. Determination of bending and torsional stiffnesses of polyester-PAA composite fibers.
Fig. S4. Cyclic tensile actuation by swelling and deswelling twisted composite fibers.
Fig. S5. Twist-induced supercoiling: Modeling and experiments.
Fig. S6. Preparation of microtools.
Fig. S7. Examples of actuated microtools.
Fig. S8. Preparation of small-diameter composite twisted fibers.
Fig. S9. Tensile actuation measurements.
Fig. S10. Torsional actuation measurements.
Fig. S11. Theoretical approach to first supercoil loop formation.
Fig. S12. Calculated potential energies comparing twist only and coiled.
Fig. S13. Experimentally measured diameter ratios of a composite two-ply samples.
Table S1. Calculation steps involved in estimating contractile stroke.
Table S2. Calculation steps involved in estimating contractile stroke.
Movie S1. Plectoneme formation and removal in twisted PAA yarn.
Movie S2. Plectoneme formation, removal, and chiral reversal in polyester-PAA loop.
Movie S3. Plectoneme formation and removal in polyester-PAA at isobaric 210 kPa.
Movie S4. Solenoid formation and removal in polyester-PAA at 900 kPa.
Movie S5. Solenoid formation and removal in PAN-PAA composite fiber.
Movie S6. Full sample view of isobaric plectoneme formation and removal in polyester-PAA composite fiber.
Movie S7. Fast plectoneme formation and removal in PAN-PAA composite fiber.
Movie S8. Multi-strand PAN-PAA actuator array.
References (*63*–*66*)

REFERENCES AND NOTES

1. J. D. Madden, Mobile robots: Motor challenges and materials solutions. *Science* **318**, 1094–1097 (2007).
2. M. Duduta, E. Hajiesmaili, H. Zhao, R. J. Wood, D. R. Clarke, Realizing the potential of dielectric elastomer artificial muscles. *Proc. Natl. Acad. Sci. U.S.A.* **116**, 2476–2481 (2019).
3. S. Sareh, J. Rossiter, Kirigami artificial muscles with complex biologically inspired morphologies. *Smart Mater. Struct.* **22**, 014004 (2013).
4. J. Foroughi, G. M. Spinks, G. G. Wallace, J. Oh, M. E. Kozlov, S. Fang, T. Mirfakhrai, J. D. Madden, M. K. Shin, S. J. Kim, R. H. Baughman, Torsional carbon nanotube artificial muscles. *Science* **334**, 494–497 (2011).
5. X. Ji, X. Liu, V. Cacucciolo, M. Imboden, Y. Civet, A. E. Haitami, S. Cantin, Y. Perriard, H. Shea, An autonomous untethered fast soft robotic insect driven by low-voltage dielectric elastomer actuators. *Sci. Robot.* **4**, eaaz6451 (2019).
6. S. W. Yeom, I. K. Oh, A biomimetic jellyfish robot based on ionic polymer metal composite actuators. *Smart Mater. Struct.* **18**, 085002 (2009).
7. J. D. W. Madden, N. A. Vandesteeg, P. A. Anquetil, P. G. A. Madden, A. Takshi, R. Z. Pytel, S. R. Lafontaine, P. A. Wieringa, I. W. Hunter, Artificial muscle technology: Physical principles and naval prospects. *IEEE J. Oceanic Eng.* **29**, 706–728 (2004).
8. A. Annunziato, DNA packaging: Nucleosomes and chromatin. *Nat. Educ.* **1**, 26 (2008).
9. L. S. Lerman, Structural considerations in the interaction of DNA and acridines. *J. Mol. Biol.* **3**, 18–30 (1961).
10. H. M. Berman, P. R. Young, The interaction of intercalating drugs with nucleic acids. *Ann. Rev. Biophys. Bioeng.* **10**, 87–114 (1981).
11. M. Hayashi, Y. Harada, Direct observation of the reversible unwinding of a single DNA molecule caused by the intercalation of ethidium bromide. *Nucleic Acids Res.* **35**, e125 (2007).
12. G. Mahipal, S. H. Kim, J. van der Torre, E. Abbondanzieri, C. Dekker, Intercalation-based single-molecule fluorescence assay to study DNA supercoil dynamics. *Nano Lett.* **16**, 4699–4707 (2016).
13. K. Gunther, M. Mertig, R. Seidel, Mechanical and structural properties of YOYO-1 complexed DNA. *Nucleic Acids Res.* **38**, 6526–6532 (2010).
14. S. M. Mirkin, DNA topology: Fundamentals, in *eLS* (John Wiley & Sons Ltd., 2001); www.els.net.
15. M. D. Lima, N. Li, M. J. de Andrade, S. Fang, J. Oh, G. M. Spinks, M. E. Kozlov, C. S. Haines, D. Suh, J. Foroughi, S. J. Kim, Y. Chen, T. Ware, M. K. Shin, L. D. Machado, A. F. Fonseca, J. D. W. Madden, W. E. Voit, D. S. Galvão, R. H. Baughman, Electrically, chemically, and photonically powered torsional and tensile actuation of hybrid carbon nanotube yarn muscles. *Science* **338**, 928–932 (2012).
16. H. H. Cheng, Y. Hu, F. Zhao, Z. L. Dong, Y. H. Wang, N. Chen, Z. P. Zhang, L. T. Qu, Moisture-activated torsional graphene-fiber motor. *Adv. Mater.* **26**, 2909–2913 (2014).
17. S. S. He, P. N. Chen, L. B. Qiu, B. J. Wang, X. M. Sun, Y. F. Xu, H. S. Peng, A mechanically actuating carbon-nanotube fiber in response to water and moisture. *Angew. Chemie Int. Ed.* **54**, 14880–14884 (2015).
18. X. Gu, Q. Fan, F. Yang, L. Cai, N. Zhang, W. Zhou, W. Zhou, S. Xie, Hydro-actuation of hybrid carbon nanotube yarn muscles. *Nanoscale* **8**, 17881–17886 (2016).
19. S. M. Mirvakili, I. W. Hunter, Fast torsional artificial muscles from NiTi twisted yarns. *ACS Appl. Mater. Interf.* **9**, 16321–16326 (2017).
20. J. Yuan, W. Neri, C. Zakri, P. Merzeau, K. Kratz, A. Lendlein, P. Poulin, Shape memory nanocomposite fibers for untethered high-energy microengines. *Science* **365**, 155–158 (2019).
21. J. Mu, M. J. de Andrade, S. Fang, X. Wang, E. Gao, N. Li, S. H. Kim, H. Wang, C. Hou, Q. Zhang, M. Zhu, D. Qian, H. Lu, D. Kongahage, S. Talebian, J. Foroughi, G. M. Spinks, H. Kim, T. H. Ware, H. J. Sim, D. Y. Lee, Y. Hang, S. J. Kim, R. H. Baughman, Sheath-run artificial muscles. *Science* **365**, 150–155 (2019).
22. D. B. Liu, A. Tarakanova, C. C. Hsu, M. Yu, S. M. Zheng, L. T. Yu, J. Liu, Y. M. He, D. J. Dunstan, M. J. Buehler, Spider dragline silk as torsional actuator driven by humidity. *Sci. Adv.* **5**, eaau9183 (2019).
23. B. Fang, Y. H. Xiao, Z. Xu, D. Chang, B. Wang, W. W. Gao, C. Gao, Handedness-controlled and solvent-driven actuators with twisted fibers. *Mater. Horiz.* **6**, 1207–1214 (2019).

24. H. Chen, H. Zhang, J. Pan, T.-G. Cha, S. Li, J. Andreasson, J. H. Choi, Dynamic and progressive control of DNA origami conformation by modulating DNA helicity with chemical adducts. *ACS Nano* **10**, 4989–4996 (2016).
25. D. J. Bell, L. X. Dong, B. J. Nelson, M. Golling, L. Zhang, D. Grützmacher, Fabrication and characterization of three-dimensional InGaAs/GaAs nanosprings. *Nano Lett.* **6**, 725–729 (2006).
26. Z. Chen, C. Majidi, D. J. Srolovitz, M. Haataja, Tunable helical ribbons. *Appl. Phys. Lett.* **98**, 011906 (2011).
27. S. Iamsaard, S. J. Asshoff, B. Matt, T. Kudernac, J. J. L. M. Cornelissen, S. P. Fletcher, N. Katsonis, Conversion of light into macroscopic helical motion. *Nat. Chem.* **6**, 229–235 (2014).
28. Z. L. Wu, M. Moshe, J. Greener, H. Therien-Aubin, Z. Nie, E. Sharon, E. Kumacheva, Three-dimensional shape transformations of hydrogel sheets induced by small-scale modulation of internal stresses. *Nat. Commun.* **4**, 1586 (2013).
29. C. S. Haines, M. D. Lima, N. Li, G. M. Spinks, J. Foroughi, J. D. W. Madden, S. H. Kim, S. Fang, M. J. de Andrade, F. Goktepe, O. Goktepe, S. Mirvakili, S. Naficy, X. Lepro, J. Oh, M. E. Kozlov, S. J. Kim, X. Xu, B. J. Swedlove, G. G. Wallace, R. H. Baughman, Artificial muscles from fishing line and sewing thread. *Science* **343**, 868–872 (2014).
30. G. Călugăreanu, Sur les classes d'isotopie des noeuds tridimensionnels et leurs invariants. *Czech. Math. J.* **11**, 588–625 (1961).
31. J. H. White, W. R. Bauer, Calculation of the twist and the writhe for representative models of DNA. *J. Molec. Biol.* **189**, 329–341 (1986).
32. F. B. Fuller, The writhing number of a space curve. *Proc. Natl. Acad. Sci. U.S.A.* **68**, 815–819 (1971).
33. D. M. Stump, W. B. Fraser, K. E. Gates, The writhing of circular cross-section rods: Undersea cables to DNA supercoils. *Proc. Roy. Soc. Lond. A* **454**, 2123–2156 (1998).
34. J. M. T. Thompson, G. M. H. van der Heijden, S. Neukrich, Supercoiling of DNA plasmids: Mechanics of the generalized ply. *Proc. Roy. Soc. Lond. A* **458**, 959–985 (2002).
35. A. Balaeff, L. Mahadevan, K. Schulten, Modeling DNA loops using the theory of elasticity. *Phys. Rev. E.* **73**, 031919 (2006).
36. I. M. Kulic, H. Mohrbach, T. Thaokar, H. Schiessel, Equation of state of looped DNA. *Phys. Rev. E* **75**, 011913 (2007).
37. N. Clauvelin, B. Audoly, S. Nuekrich, Mechanical response of plectonemic DNA: An analytical solution. *Macromol.* **41**, 4479–4483 (2008).
38. A. G. Cherstvy, Torque-induced deformations of charged elastic DNA rods: Thin helices, loops, and precursors of DNA supercoiling. *J. Biol. Phys.* **37**, 227–238 (2011).
39. P.-M. Lam, Y. Zhen, Extension, torque, and supercoiling in single, stretched, and twisted DNA molecules. *J. Chem. Phys.* **143**, 176901 (2015).
40. A. L. Ross, Cable kinking analysis and prevention. *Trans. J. Eng. Ind.* **99**, 112–115 (1977).
41. J. Coyne, Analysis of the formation and elimination of loops in twisted cable. *J. Oceanic Eng.* **15**, 72–83 (1990).
42. R. L. Ricca, The energy spectrum of a twisted flexible string under elastic relaxation. *J. Phys. A Math. Gen.* **28**, 2335–2352 (1995).
43. J. M. T. Thomson, A. R. Champneys, From helix to localized writhing in the torsional post-buckling of elastic rods. *Proc. Roy. Soc. Lond. A* **452**, 117–138 (1996).
44. A. Goriely, M. Tabor, Nonlinear dynamics of filaments. IV Spontaneous looping of twisted elastic rods. *Proc. Roy. Soc. Lond. A* **454**, 3183–3202 (1998).
45. G. M. H. van der Heijden, J. M. T. Thomoson, Helical and localised buckling in twisted rods: A unified analysis of the symmetric case. *Nonlin. Dyn.* **21**, 71–99 (2000).
46. A. N. Gent, K.-C. Hua, Torsional instability of stretched rubber cylinders. *Int. J. Non Linear Mech.* **39**, 483–489 (2004).
47. A. Ghatak, L. Mahadevan, Solenoids and plectonemes in stretched and twisted elastomeric filaments. *Phys. Rev. Lett.* **95**, 057801 (2005).
48. P. K. Purohit, Plectoneme formation in twisted fluctuating rods. *J. Mech. Phys. Solids* **56**, 1715–1729 (2008).
49. N. Charles, M. Gazzola, L. Mahadevan, Topology, geometry, and mechanics of strongly stretched and twisted filaments: Solenoids, Plectonemes, and artificial muscle fibers. *Phys. Rev. Lett.* **123**, 208003 (2019).
50. S. H. Kim, C. H. Kwon, K. Park, T. J. Mun, X. Lepró, R. H. Baughman, G. M. Spinks, S. J. Kim, Bio-inspired, moisture-powered hybrid carbon nanotube yarn muscles. *Sci. Rep.* **6**, 23016 (2016).
51. T. Jia, Y. Wang, Y. Dou, Y. Li, M. J. de Andrade, R. Wang, S. Fang, J. Li, Z. Yu, R. Qiao, Z. Liu, Y. Cheng, Y. Su, M. Minary-Jolandan, R. H. Baughman, D. Qian, Z. Liu, Moisture sensitive smart yarns and textiles from self-balanced silk fiber muscles. *Adv. Funct. Mater.* **29**, 1808241 (2019).
52. P. Chen, Y. Xu, S. He, X. Sun, S. Pan, J. Deng, D. Chen, H. Peng, Hierarchically arranged helical fiber actuators driven by solvents and vapours. *Nat. Nanotechnol.* **10**, 1077–1083 (2015).
53. S. Kimuro, A. Kirishima, N. Sato, Determination of the protonation enthalpy of humic acid by calorimetric titration technique. *J. Chem. Thermodyn.* **82**, 1–8 (2015).
54. N. Kellaris, V. G. Venkata, G. M. Smith, S. K. Mitchell, C. Keplinger, Peano-HASEL actuators: Muscle-mimetic, electrohydraulic transducers that linearly contract on activation. *Sci. Robot.* **3**, eaar3276 (2018).
55. C. Laschi, B. Mazzolai, M. Cianchetti, Soft robotics: Technologies and systems pushing the boundaries of robot abilities. *Sci. Robot.* **1**, eaah3690 (2016).
56. L. Wu, M. J. de Andrade, L. K. Saharan, R. S. Rome, R. H. Baughman, Y. Tadesse, Compact and low-cost humanoid hand powered by nylon artificial muscles. *Bioinspir. Biomim.* **12**, 026004 (2017).
57. A. Yara, Y. Tadesse, Twisted and coiled polymer (TCP) muscles embedded in silicone elastomer for use in soft robot. *Int. J. Intell. Robot. Appl.* **1**, 352–368 (2017).
58. J. F. Sun, B. Tighe, Y. X. Liu, J. G. Zhao, Twisted-and-coiled actuators with free strokes enable soft robots with programmable motions. *Soft Robot* 10.1089/soro.2019.0175 (2020).
59. P. Fratzl, F. G. Barth, Biomaterial systems for mechanosensing and actuation. *Nature* **462**, 442–448 (2009).
60. A. Upadhyaya, M. Baraban, J. Wong, P. Matsudaira, A. van Oudenaarden, L. Mahadevan, Power-limited contraction dynamics of *Vorticella convallaria*: An ultrafast biological spring. *Biophys. J.* **94**, 265–272 (2008).
61. A. J. Bowling, K. C. Vaughn, Gelatinous fibers are widespread in coiling tendrils and twining vines. *Am. J. Botany* **96**, 719–727 (2009).
62. C. Cuveiller, J. Delaroche, M. Seggio, S. Gory-Fauré, C. Bosc, E. Denarier, M. Bacia, G. Schoehn, H. Mohrbach, I. Kulic, A. Andrieux, I. Arnal, C. Delphin, MAP6 is an intraluminal protein that induces neuronal microtubules to coil. *Sci. Adv.* **6**, eaaz4344 (2020).
63. A. G. Greenhill, On the strength of shafting when exposed to torsion and end thrust. *Proc. Inst. Mech. Eng.* **34**, 182–209 (1883).
64. E. B. Belov, S. V. Lomov, N. N. Truevtsev, M. Bradshaw, R. Harwood, Measurement of the rorsional strength of chemical fibres and critical parameters of formation of snarls. *Fiber Chem.* **31**, 380–386 (1999).
65. C. Zhao, Q. Liu, L. Ren, Z. Song, J. Wang, A 3D micromechanical study of hygroscopic coiling deformation in Pelargonium seed: From material and mechanics perspective. *J. Mater. Sci.* **52**, 415–430 (2017).
66. A. S. Biebricher, I. Heller, R. F. H. Roijmans, T. P. Hoekstra, E. J. G. Peterman, G. J. L. Wuite, The impact of DNA intercalators on DNA and DNA-processing enzymes elucidated through force-dependent binding kinetics. *Nat. Commun.* **6**, 7304 (2015).

Funding: G.M.S. received funding support through University of Wollongong's Global Challenges Program. **Author contributions:** N.D.M. and G.M.S. conducted experiments with assistance from D.J.S. and J.F. Data was analyzed by G.M.S. and modeled by G.M.S. and S.N. G.M.S. wrote the paper, and all authors reviewed the manuscript. **Competing interests:** The authors declare that they have no competing interests. **Data and materials availability:** All data are available in the main text or the Supplementary Materials.

Submitted 29 October 2020
Accepted 6 April 2021
Published 28 April 2021
10.1126/scirobotics.abf4788

Citation: G. M. Spinks, N. D. Martino, S. Naficy, D. J. Shepherd, J. Foroughi, Dual high-stroke and high–work capacity artificial muscles inspired by DNA supercoiling. *Sci. Robot.* **6**, eabf4788 (2021).

Dual high-stroke and high–work capacity artificial muscles inspired by DNA supercoiling

Geoffrey M. Spinks, Nicolas D. Martino, Sina Naficy, David J. Shepherd and Javad Foroughi

Sci. Robotics **6**, eabf4788.
DOI: 10.1126/scirobotics.abf4788